

PONTIFICIA UNIVERSIDAD CATÓLICA DEL PERÚ

FACULTAD DE CIENCIAS E INGENIERÍA



PUCP

Estudio de un magnetrón utilizando el método de elementos finitos

TRABAJO DE INVESTIGACIÓN PARA OBTENER EL GRADO ACADÉMICO DE BACHILLER EN CIENCIAS CON MENCIÓN EN FÍSICA

AUTOR

Erik Alfredo Pérez Caro

ASESOR

Humberto Torreblanca Quiroz, PhD

École Polytechnique Fédérale de Lausanne

Lima, 15 de enero de 2021

Abstract

Magnetron sputtering system is a technique that consists in extracting atoms from a target material by collisions of energetic ions of an inert gas. It is widely used in semiconductor industries and materials processing research for developing thin films by deposition. During this process a low temperature capacitively coupled plasma is generated near the cathode and several variations of the properties of this plasma can affect the thin film deposition process and quality. An approach to study these types of systems is by computational modeling. The use of robust computational codes that can handle complicated geometries and can solve complex systems of differential equations. In this present project we aim to model numerically a system of magnetrons developed at the Materials Science and Renewable Energies (MatER) laboratory. Using the geometry measurements and the material properties of each component taken in the laboratory, a CAD geometry was developed. Furthermore, the electric and magnetic fields are solved for the geometry configuration and, by implementing a Monte Carlo simulation, the electron trajectories and velocity distributions in the system are calculated. Finally, we use a multi-fluid model to solve a simplified system of a 1 dimensional capacitively coupled plasma and recover the system properties. The method to solve the respective system of equations is the finite element method implemented in the software COMSOL Multiphysics.

Table of contents

Abstract	I
Table of contents	II
List of Figures	III
List of Tables	IV
I. Introduction	1
II. Theory	3
2.1. Maxwell's Equations	3
2.2. Single Particle Motions	5
2.2.1. Uniform \mathbf{E} and \mathbf{B} fields with $\mathbf{E} = \mathbf{0}$	5
2.2.2. Uniform \mathbf{E} and \mathbf{B} fields with $\mathbf{E} \neq \mathbf{0}$	6
2.2.3. Nonuniform \mathbf{E} and \mathbf{B} fields with $\mathbf{E} = \mathbf{0}$	8
2.2.4. Nonuniform \mathbf{E} field	9
2.3. Plasmas as Fluids	10
III. Numerical Simulations	12
3.1. Design	12
3.2. Mesh Study	14
3.2.1. Parametric Sweep	16
3.2.2. Mesh Study Results	16
3.3. Results	23
3.3.1. Electric Potential and Electric Field	23
3.3.2. Magnetic Field	25
3.3.3. Particle Trajectories	26
3.3.4. Fluid simulation of a capacitively coupled plasma	32
IV. Conclusions	37
Bibliography	39

List of Figures

2.1. Ion (red) and negative (blue) charge trajectories in uniform E and B fields	8
3.1. CAD design of a magnetron	13
3.2. Ground Powered Electrodes	13
3.3. Neodymium Magnets	14
3.4. Geometry selection around the magnetron	15
3.5. Mesh visualization with sizes between (1E-8 m , 9.5E-4 m)	16
3.6. Geometry points to evaluate electromagnetic variables	17
3.7. Electric potential (V) evaluated in four points	17
3.8. Electric field norm (E) evaluated in four points	18
3.9. Magnetic scalar potential evaluated in four points	19
3.10. Magnetic field evaluated in four points	20
3.11. Error of the solutions vs mesh size for the electric potential and the magnetic scalar potential	21
3.12. Execution time and degrees of freedom vs mesh size	21
3.13. Final mesh size	22
3.14. Electric potential distribution	24
3.15. Electric field distribution	24
3.16. Magnetic field norm distribution	25
3.17. Electron transport in the surface of the target due the Hall Effect	27
3.18. Cut plane at $z = 0.276$ m and the Poincaré map of electron trajectories	27
3.19. Argon cross sections for elastic, excitation and ionization reactions [19]	29
3.20. System of three magnetrons	31
3.21. Electrons velocity distribution	32
3.22. Diagram of a CCP [22]	33
3.23. Electron density profile as a function of the distance	34
3.24. Electron temperature profile as a function of the distance	35
3.25. Electric potential and electric field profiles as a function of the distance	35

List of Tables

3.1. Table of permittivity and permeability of materials [11]	14
3.2. Table of mesh study parameters and results	22
3.3. Collision types considered in the particle simulation [17]	28



Chapter I

Introduction

Sputtering is a process where particles from a solid material called target are ejected from its surface by the collisions of energetic ions with the target material. These energetic ions are generated by the ionization of an inert gas like Argon, and the ionization occurs due to the high intensity electric field. This field then separates charges and, particles in the gas move around until they collide with each other [1]. The electric field is generated by a magnetron, a device that consists of a pair of electrodes in a cylindrical configuration, one electrode is powered by a radio frequency source operating with a maximum amplitude of 195 V and a RF electric field is generated between these two electrodes. Additionally, the magnetron has an internal pair of toroidally-shaped permanent magnets. These magnets generate a poloidal magnetic field with the purpose to confine electrons and ions around the target. When the electric field is strong enough to separate the electrons from the atoms of the inert gas, the free ions and electrons heat the gas by colliding with the gas particles until an electrical or plasma discharge is produced between the electrodes [2]. A plasma is a quasi-neutral gas, where microscopically positive and negative charges are separated and move freely, while macroscopically the gas is neutral. After a certain time, when a considerable amount of collisions between electrons, ions and neutral particles have occurred, the plasma is self-sustainable. This ionized gas has a collective behavior which allows it to be driven and confined by electric and magnetic fields [3]. The

plasma produces the energetic ions that are accelerated and then extract the target material. The extracted or sputtered particles are vaporized and conducted to a substrate where they are deposited to form a thin film [2].

The finite element method (FEM) is a numerical method to solve systems of partial differential equations (PDEs). This method consists of defining a set of base functions or elements, and then multiplying these elements by random weights to construct possible solutions to the set of dependent variables. Then a system of linear equations is solved to find the optimum weights that solve the set of PDEs [4]. For this project, the software COMSOL Multiphysics, which implements the finite element method, has been used.

In this present project we aim to model numerically a system of magnetrons using geometry measurements taken at the laboratory. In Chapter II we present the theory behind the computational simulations: Maxwell's equations, motion of charged particles and plasmas as fluids. In Chapter III, we show the simulation results: numerical error study, electric and magnetic field spatial configuration results, electron trajectories and the capacitively coupled plasma simulation. In Chapter IV a conclusion and final remarks are presented.

Chapter II

Theory

2.1. Maxwell's Equations

Maxwell's equations has to be solved with certain conditions to numerically solve the electric field generated by two electrodes and the magnetic field generated a magnet:

$$\begin{aligned}\nabla \times \mathbf{H} &= \mathbf{J} + \frac{\partial \mathbf{D}}{\partial t} \\ \nabla \times \mathbf{E} &= -\frac{\partial \mathbf{B}}{\partial t} \\ \nabla \cdot \mathbf{D} &= \rho \\ \nabla \cdot \mathbf{B} &= 0\end{aligned}\tag{2.1}$$

The electrodes that are part of the magnetron used in the laboratory are made of 304 stainless steel, a conductive material. To describe the electric field produced by the potential applied to the boundary of this electrode we need to consider the third Maxwell's equation and use the gradient of the electric potential $\mathbf{E} = -\nabla V$ in (V/m). We get the following equations:

$$\begin{aligned}\epsilon_0 \epsilon_r \nabla \cdot \mathbf{E} &= \rho \\ \mathbf{E} &= -\nabla V\end{aligned}\tag{2.2}$$

Where ϵ_0 y ϵ_r are the electrical permittivity of vacuum and the relative electrical permittivity of the material where the field is calculated. To solve this system we need to establish the initial boundary conditions that are determined by the geometry of the problem and the value of the potential $V(x,y,z,t)$ at each point in the geometry at every time.

A magnet is an object made of a ferromagnetic material; it produces a magnetic field with no current involved. To model a magnet's magnetic field we need to establish a set of equations that involve a medium with no currents or a time dependent electric field. So we start with the first Maxwell's equation:

$$\nabla \times \mathbf{H} = 0 \quad (2.3)$$

It is convenient to define the magnetic field vector as the gradient of a magnetic scalar potential.

$$\mathbf{H} = -\nabla V_m \quad (2.4)$$

Also, for permanent magnets a magnetization vector \mathbf{M} needs to be defined in some preferred direction. Finally, the system of equations to be solved simultaneously is:

$$\begin{aligned} \nabla \cdot \mathbf{B} &= 0 \\ \mathbf{B} &= \mu_0(\mu_r \mathbf{H} + \mathbf{M}) \\ \mathbf{H} &= -\nabla V_m \end{aligned} \quad (2.5)$$

Where μ_0 and μ_r are the magnetic permeability of vacuum and the relative magnetic permeability of the material. The input parameter of the model is the magnetization vector \mathbf{M} as a domain condition. It describes how the object is magnetized in direction and magnitude. This condition will determine the magnetic field distribution in all the domains [5].

2.2. Single Particle Motions

The trajectory of a charged particle in the presence of an electric field and a magnetic field is determined by Newton's law in which the force acting on the particle of mass m and charge q is given by the Lorentz force:

$$m \frac{d\mathbf{v}}{dt} = q(\mathbf{E} + \mathbf{v} \times \mathbf{B}) \quad (2.6)$$

The fields are described by the vectors \mathbf{E} and \mathbf{B} . This equation describes completely the trajectory of a particle in any electromagnetic system. The complexity of describing these fields arises when there are no analytical solutions available. To understand the movement of charged particles in a plasma, we will study particular cases and semi-analytical solutions to eq. 2.6. It should be emphasized that in these particular cases the fields will be described when they are generated by external sources to the plasma and not by the spatial distribution of charges [6].

2.2.1. Uniform \mathbf{E} and \mathbf{B} fields with $\mathbf{E} = \mathbf{0}$

Taking $\mathbf{E} = \mathbf{0}$ in equation 2.6 we obtain:

$$m \frac{d\mathbf{v}}{dt} = q\mathbf{v} \times \mathbf{B} \quad (2.7)$$

We consider the magnetic field to be oriented in the \hat{z} direction $\mathbf{B} = B\hat{z}$. The resulting differential equations for the velocities v_x and v_y are:

$$\begin{aligned} \ddot{v}_x &= -\left(\frac{qB}{m}\right)^2 v_x \\ \ddot{v}_y &= -\left(\frac{qB}{m}\right)^2 v_y \end{aligned} \quad (2.8)$$

The solution is of a simple harmonic oscillator with cyclotron frequency

$$\omega_c \equiv \frac{|q|B}{m}$$

and the law of motion

$$\begin{aligned}x(t) &= x_0 + r_L \sin \omega_c t \\y(t) &= y_0 \pm r_L \cos \omega_c t\end{aligned}\tag{2.9}$$

where r_L is the Larmor radius and is defined as

$$r_L \equiv \frac{v_{\perp}}{\omega_c} = \frac{mv_{\perp}}{|q|\mathbf{B}}\tag{2.10}$$

Where $v_{\perp} = \sqrt{v_x^2 + v_y^2}$ is the velocity magnitude perpendicular to the magnetic field. The trajectory describes a circular motion around the center (x_0, y_0) with radius r_L [6].

2.2.2. Uniform \mathbf{E} and \mathbf{B} fields with $\mathbf{E} \neq \mathbf{0}$

If we consider a constant and uniform electric field \mathbf{E} , the equation of motion is described by:

$$m \frac{d\mathbf{v}}{dt} = q(\mathbf{E} + \mathbf{v} \times \mathbf{B})\tag{2.11}$$

Let's consider that the \mathbf{E} field lies in the x-y plane and \mathbf{B} has only a component in the \hat{z} direction, then the solution to velocity in \hat{z} is given by:

$$\begin{aligned}\frac{dv_z}{dt} &= 0 \\v_z &= v_{z0}\end{aligned}\tag{2.12}$$

The differential equations for the x and y directions are:

$$\begin{aligned}\frac{dv_x}{dt} &= \frac{q}{m} E_x \pm \omega_c v_y \\ \frac{dv_y}{dt} &= \frac{q}{m} E_y \mp \omega_c v_x\end{aligned}\tag{2.13}$$

Where the sign depends on the particle's charge. Differentiating both equations we have:

$$\begin{aligned}\ddot{v}_x &= \frac{d^2}{dt^2} \left(v_x - \frac{E_y}{B} \right) = -\omega_c^2 \left(v_x - \frac{E_y}{B} \right) \\ \ddot{v}_y &= \frac{d^2}{dt^2} \left(v_y + \frac{E_x}{B} \right) = -\omega_c^2 \left(v_y + \frac{E_x}{B} \right)\end{aligned}\tag{2.14}$$

The solution to this pair of differential equations is:

$$\begin{aligned}v_x &= v_{\perp} \cos \omega_c t + \frac{E_y}{B} \\ v_y &= v_{\perp} \sin \omega_c t - \frac{E_x}{B}\end{aligned}\tag{2.15}$$

The velocity can be separated in two components, one component describes the cyclotron motion of the particle and the other component can be written as:

$$\begin{aligned}\mathbf{v}_E &= \left(\frac{E_y}{B}, -\frac{E_x}{B}, 0 \right) \\ \mathbf{v}_E &= \frac{\mathbf{E} \times \mathbf{B}}{\|\mathbf{B}\|^2}\end{aligned}\tag{2.16}$$

This component is known as the $\mathbf{E} \times \mathbf{B}$ drift, it describes the movement of the gyro-center of the particle in the direction perpendicular to both fields. This velocity is independent of the mass and charge of the particle so all species in a plasma will drift in the same direction due to this effect [6]. To visualize this effect, we can numerically simulate the trajectories of a positive ion and a negative charge with the ion heavier than the negative charge. We impose a magnetic field in the \hat{z} direction and an electric field in the \hat{x} direction:

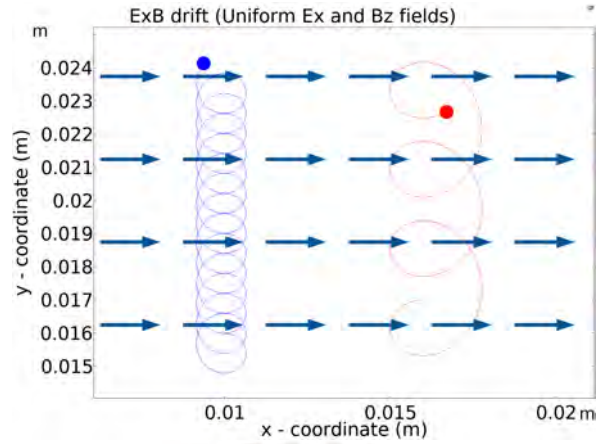


Figure 2.1: Ion (red) and negative (blue) charge trajectories in uniform E and B fields

The drift velocity as predicted in 2.16 is in the \hat{y} direction and both particles drift in the same direction. The theoretical value of the $\mathbf{E} \times \mathbf{B}$ drift calculated using equation 2.16 agrees well with the numerical value determined using COMSOL.

2.2.3. Nonuniform E and B fields with $\mathbf{E} = \mathbf{0}$

In this case the magnetic field is nonuniform, now it has a spatial dependence $\mathbf{B} = \mathbf{B}(x, y, z)$. From equation 2.7, since the field depends on the position and the solution to the position of the particle changes in time, \mathbf{B} will have to be recalculated at each time for different coordinates. Let's consider that the magnetic field only has a component in the \hat{z} direction and the variation of the field occurs in the \hat{y} direction, then the force is given by:

$$\vec{\mathbf{F}} = q(\mathbf{v} \times \mathbf{B}) = q[v_y B_z(y), -v_x B_z(y), 0] \quad (2.17)$$

$$F_y = -qv_x B_z(y) \quad (2.18)$$

To find an approximate solution, a perturbative analysis of the magnetic field can be performed. We make a Taylor expansion of the \mathbf{B} field around $x_0 = 0$ and $y_0 = 0$ and replace the solution of

v_x obtained from 2.9:

$$F_y = -qv_{\perp} \cos \omega_c t \left(B_0 \pm r_L \cos \omega_c t \frac{\partial B_z}{\partial y} \right) \quad (2.19)$$

To determine the displacement of the gyrocenter we take the average to the expression 2.19:

$$\bar{F}_y = \mp qv_{\perp} r_L \frac{1}{2} \frac{\partial B_z}{\partial y} \quad (2.20)$$

We can express the drift due a general force \mathbf{F} as:

$$\mathbf{v}_c = \frac{1}{q} \frac{\mathbf{F} \times \mathbf{B}}{\|\mathbf{B}\|^2} = \mp \frac{1}{\|\mathbf{B}\|} v_{\perp} r_L \frac{1}{2} \frac{\partial B_z}{\partial y} \hat{x} \quad (2.21)$$

Then, the drift due to the gradient of the magnetic field, also called ∇B drift, is calculated as follows

$$\mathbf{v}_{\nabla B} = \pm \frac{1}{2} v_{\perp} r_L \frac{\mathbf{B} \times \nabla B}{\|\mathbf{B}\|^2} \quad (2.22)$$

This drift velocity is generated in the presence of a nonuniform magnetic field and is perpendicular to the direction of the field and the direction of the gradient of the field. Furthermore, it depends on the sign of the charge, therefore this effect generates charge separation and a current perpendicular to \mathbf{B} [6].

2.2.4. Nonuniform \mathbf{E} field

The presence of a spatial dependent electric \mathbf{E} field will generate a drift velocity in the particles of a plasma. The derivation of the drift velocity expression will be avoided, it can be found in *Introduction to Plasma Physics and Controlled Fusion* page 35. The nonuniform \mathbf{E} drift has the form:

$$\mathbf{v}_E = \left(1 + \frac{1}{4} r_L^2 \nabla^2 \right) \frac{\mathbf{E} \times \mathbf{B}}{\|\mathbf{B}\|^2} \quad (2.23)$$

It is an expression similar to the $\mathbf{E} \times \mathbf{B}$ drift only that there is a correction factor that involves the charge and mass of the particle. This effect also generates a charge separation between electrons and ions, hence, a current [6].

2.3. Plasmas as Fluids

The description of plasmas can be separated in two main formalisms. On one hand, it can be described by solving the particle trajectories and velocities at each time t , and then recovering the main variables such as density and temperature. However, this approach is almost impossible to carry out since millions of particles would have to be simulated. On the other hand, plasmas can be described statistically by taking global and collective variables of each species in the gas. The evolution of all the species in time can be described by a distribution function that describes all the particles macroscopic properties in phase space and time. The distribution function f obeys the following differential equation, also called the Boltzmann equation.

$$\frac{\partial f}{\partial t} + \mathbf{v} \cdot \nabla f + \frac{\mathbf{F}}{m} \cdot \nabla_{\mathbf{v}} f = \frac{\delta_c f}{\delta t} \quad (2.24)$$

This equation is the basis for describing all types of plasmas, it captures different types of phenomena in different range scales [7]. The left-hand side describes the long-range interactions between particles and the respective fields involved, while the right-hand side describes short range collisional interactions between particles [8]. To make a simplified model one can take the first three moments of the Boltzmann equation and describe the system with three main macroscopic quantities: density, mean velocity and mean energy of the constituent species [9].

Equation 2.24 is applied to each species or type of particle in the gas, so we can represent the distribution function f as f_s , where s indicates the species. The zeroth moment or mass

equation is obtained by multiplying eq. 2.24 by v^0 and integrating throughout the volume.

$$\int_V \frac{\partial f_s}{\partial t} d^3\mathbf{v} + \int_V \mathbf{v} \cdot \nabla f_s d^3\mathbf{v} + \int_V \frac{\mathbf{F}}{m} \cdot \nabla_{\mathbf{v}} f_s d^3\mathbf{v} = \int_V \frac{\delta_c f_s}{\delta t} d^3\mathbf{v} \quad (2.25)$$

$$\frac{\partial n_s}{\partial t} + \nabla \cdot n_s \mathbf{V}_s = 0$$

Here n_s and \mathbf{V}_s are the density and the mean velocity of the species s respectively. The first moment or momentum equation is obtained by multiplying eq. 2.24 by $m_s \mathbf{v}$ and integrating throughout the volume.

$$m_s \int_V \mathbf{v} \frac{\partial f_s}{\partial t} d^3\mathbf{v} + m_s \int_V \mathbf{v} (\mathbf{v} \cdot \nabla f_s) d^3\mathbf{v} + m_s \int_V \mathbf{v} \left(\frac{\mathbf{F}}{m_s} \cdot \nabla_{\mathbf{v}} f_s \right) d^3\mathbf{v} = m_s \int_V \mathbf{v} \frac{\delta_c f_s}{\delta t} d^3\mathbf{v} \quad (2.26)$$

$$m_s n_s \frac{d\mathbf{V}_s}{dt} = n_s e_s [\mathbf{E} + \mathbf{V}_s \times \mathbf{B}] - \nabla \cdot \vec{\mathbf{P}}_s + \frac{\delta_c \vec{\mathbf{P}}_s}{\delta t}$$

Here \mathbf{E} and \mathbf{B} are the electric and magnetic fields that affects all of the species in the plasma and $\vec{\mathbf{P}}_s$ is the pressure tensor of the species s . The second moment or the energy equation is obtained by multiplying eq. 2.24 by the kinetic energy $\frac{1}{2} m_s v_s^2$.

$$\frac{m_s}{2} \int_V \mathbf{v}^2 \frac{\partial f_s}{\partial t} d^3\mathbf{v} + \frac{m_s}{2} \int_V \mathbf{v}^2 (\mathbf{v} \cdot \nabla f_s) d^3\mathbf{v} + \frac{m_s}{2} \int_V \mathbf{v}^2 \left(\frac{\mathbf{F}}{m_s} \cdot \nabla_{\mathbf{v}} f_s \right) d^3\mathbf{v} = \frac{m_s}{2} \int_V \mathbf{v}^2 \frac{\delta_c f_s}{\delta t} d^3\mathbf{v}$$

$$\frac{\partial W_s}{\partial t} + \nabla \cdot \mathbf{Q}_s - \mathbf{E} \cdot \mathbf{J}_s = \int_V \frac{1}{2} m_s \mathbf{v}^2 \frac{\delta_c f}{\delta t} d^3\mathbf{v} \quad (2.27)$$

In this case W_s is the kinetic energy density, \mathbf{Q}_s is the kinetic energy flux and \mathbf{J}_s is the current density of the species s [8]. These three equations represent the mass conservation, moment conservation and energy conservation of the system. A more complicated version of this system is implemented in COMSOL Multiphysics as part of its computational plasma fluid code [10].

Chapter III

Numerical Simulations

3.1. Design

The magnetron sputtering system operating at the Materials Science and Renewable Energies (MatER) laboratory consists of three magnetrons pointing towards a substrate. A magnetron is a cylindrical shaped device with a pair of electrodes, a refrigeration system to cool down the temperature of the device and a pair of cylindrical and toroidal shaped magnets. The dimensions of the magnetrons in the laboratory are approximately 3.15 cm of radius and 8.032 cm of height. In the following figures we show the schematic construction of the CAD geometry in two and three dimensions:

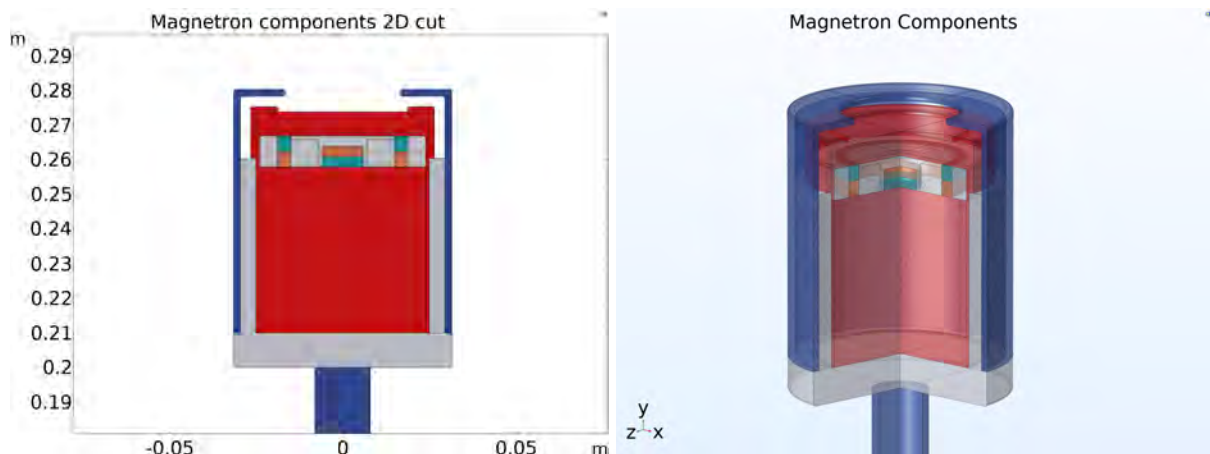


Figure 3.1: CAD design of a magnetron

In red color is shown the electrode connected to the RF power supply of 10-120 W and 13.56 MHz. In blue color is shown the electrodes connected to ground and in gray are the insulator materials and the refrigeration conducts where the cooling water passes. In orange is shown the north pole and in green the south pole of the neodymium magnets. To see the components in a more detailed version we plot the electrodes by separate:

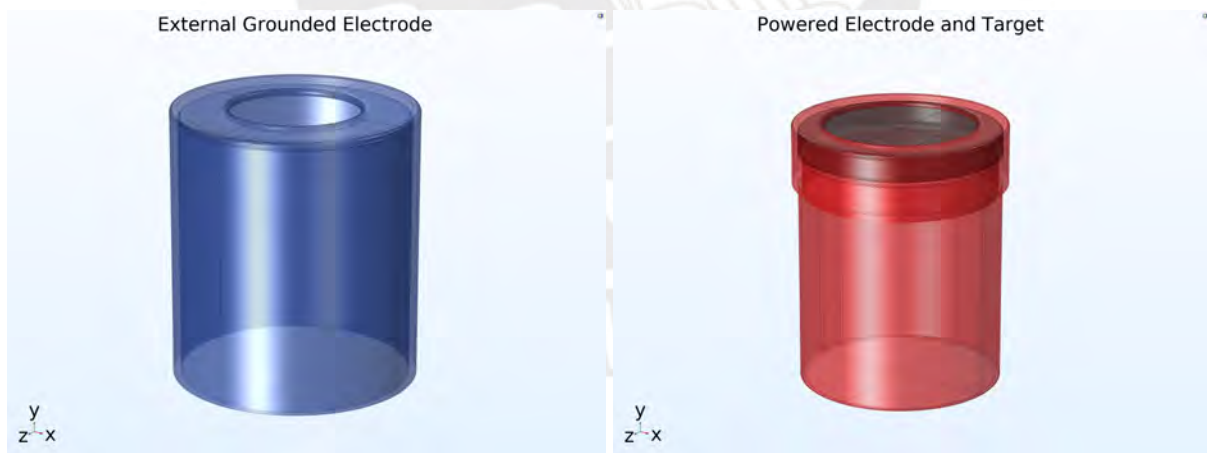


Figure 3.2: Ground Powered Electrodes

On the left we have the external ground electrode, on the right the internal powered electrode and in black is shown the target material. In the next image we show the magnets in a 3D plot:

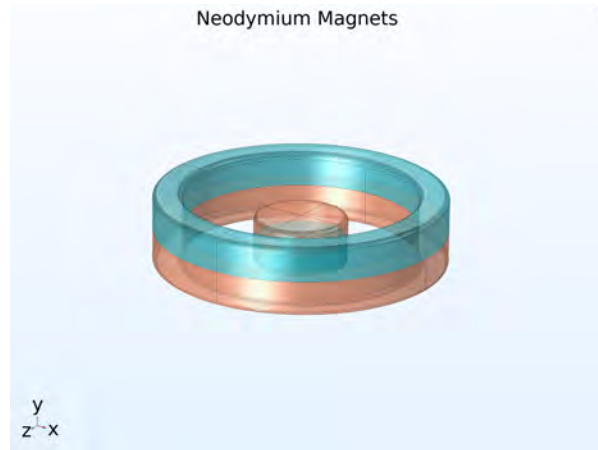


Figure 3.3: Neodymium Magnets

As we are modeling electric and magnetic fields in different mediums, to solve Maxwell's equations we require the material properties such as the electrical permittivity and the magnetic permeability. In the next table we show the values used in the respective simulations.

Material	Relative Permittivity (ϵ_r)	Relative Permeability (μ_r)
Argon	1.0	0.99
304 Stainless Steel	1.002	1
Teflon	2.1	1
Water	60	1
Silicon	11.7	0.9983
Neodymium	1	1.05

Table 3.1: Table of permittivity and permeability of materials [11]

3.2. Mesh Study

Since we do not have an analytical solution to the system of partial differential equations that determines the value of the electric and magnetic fields, particle trajectories or the fluid

equations at each point in the vacuum chamber we must numerically analyze the solutions at different points and vary the mesh element sizes to statistically establish which is the closest solution to the real value. As the mesh is a discrete partition of space, it is permissible to think that reducing the mesh element sizes to the minimum numerical size possible will give the most accurate solution but, as will be shown, due to numerical stability conditions there is a minimum mesh element size to which solutions can be acceptable. Other reasons for which it is not necessary to minimize the partition size are the computational cost, available RAM memory, hard disk drive (HDD) memory, and the execution time of the model.

We will perform a mesh study in a two dimensional cut of the magnetron sputtering system and in the full three dimensional geometry. The mesh element size will be varied until seeing a point where the solutions are independent of the partition size or until the margin of error is less than a small ϵ value.

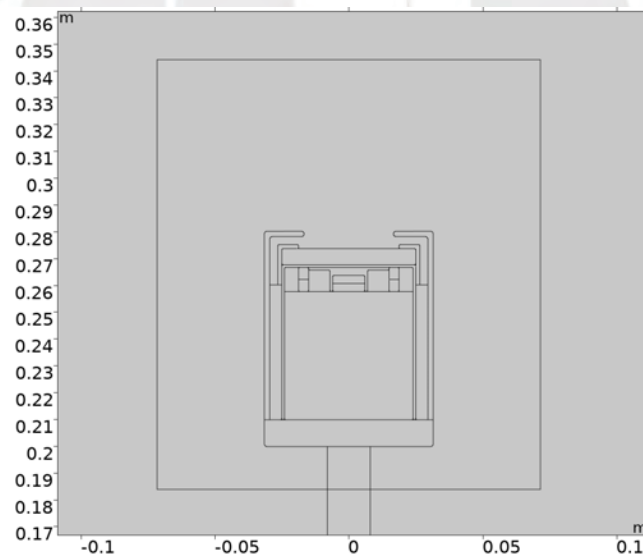


Figure 3.4: Geometry selection around the magnetron

We select a small region of space that surrounds the magnetron, see figure 3.4, because in this region the mesh will be varied to very small sizes, if we apply the same size to the entire camera, the study and simulations would take much longer and would be unnecessary. The solutions to the electric and magnetic fields, and the particle trajectories are more relevant in

this region, near the target. To have the right description we calculate the solutions for very small and very large mesh element sizes.

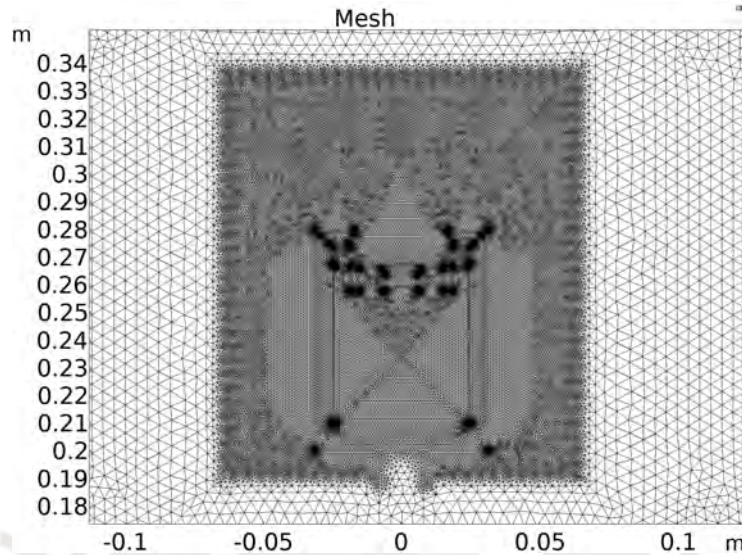


Figure 3.5: Mesh visualization with sizes between (1E-8 m , 9.5E-4 m)

3.2.1. Parametric Sweep

To conduct a mesh study, we use COMSOL's study option Parametric Sweep for different mesh element sizes and then analyze the relationship between the size and solutions. We used 160 mesh element sizes between $3.7e-4$ m and 0.04 m.

3.2.2. Mesh Study Results

We select several data points in the geometry near the target and evaluate the electric field, magnetic field, electric potential and the scalar magnetic potential in these points and study their values as we vary the mesh size.

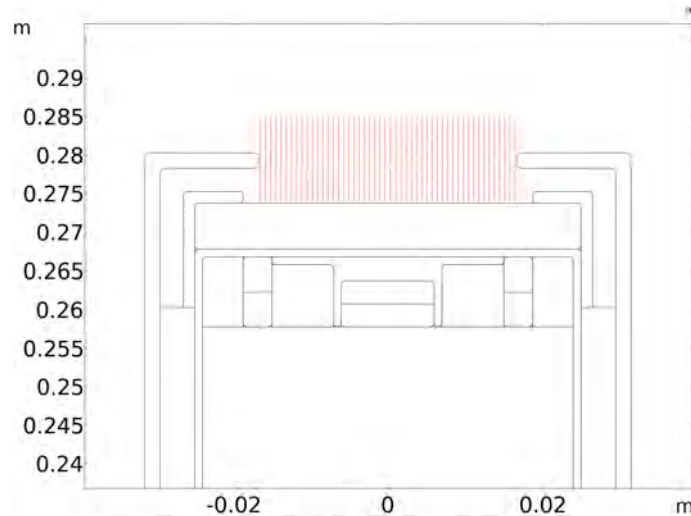


Figure 3.6: Geometry points to evaluate electromagnetic variables

We first calculate the electric potential in the data set and vary the mesh element size. Electric potential values for four points with coordinates $(-0.1, 28.5)$ cm (blue), $(0.03, 28.5)$ cm (green), $(1.68, 28.5)$ cm (red) and $(2.35, 28.5)$ cm (cyan) in the data set are shown:

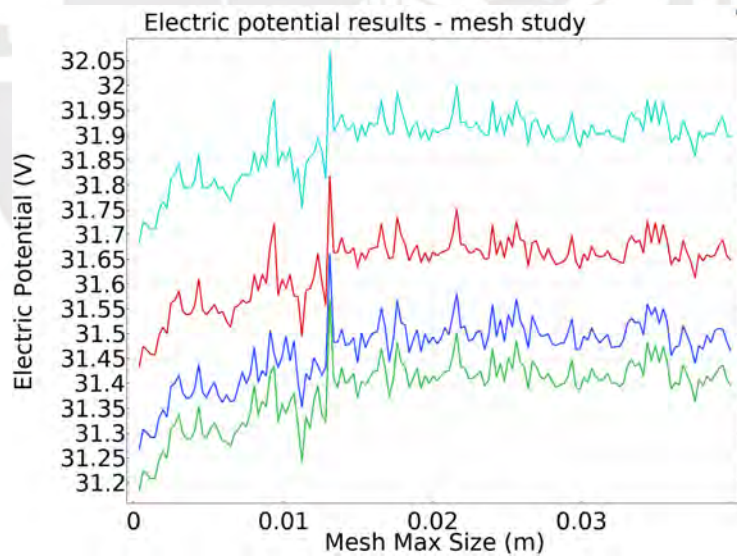


Figure 3.7: Electric potential (V) evaluated in four points

As we can observe, the values of the electric potential (V) for mesh size greater than 0.015 m reach an approximately constant value independent of the mesh size with some noise in the solutions. On the other hand, for values smaller than 0.015 m the values start to drop and the

error increases. The mean of the standard deviation values of the electric potential evaluated at all points for mesh sizes smaller than 0.015 m is 0.052 and for values greater than 0.015 m the standard deviation is 0.013. As we can observe the error decreases for values greater than 0.015 m.

Second, we calculate the electric field in the data set and vary the mesh element size. Electric field values for four points with coordinates (1.6, 27.4) cm (cyan), (1.58, 27.4) cm (blue), (1.59, 27.4) cm (green) and (1.57, 27.4) cm (red) in the data set are shown:

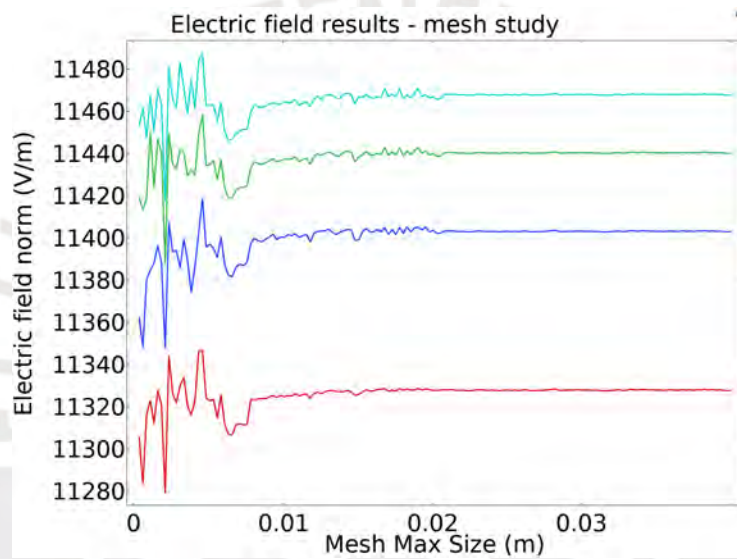


Figure 3.8: Electric field norm (E) evaluated in four points

In this case, the error as the mesh size decrements increases considerably. From the value of 0.02 m to 0.04 m the calculations of $\|E\|$ remain almost constant. The mean of the standard deviation values of the electric field norm evaluated at all points for mesh sizes smaller than 0.02 m is 11.5 and for sizes greater than 0.02 m the standard deviation is 0.6.

Third, we calculate the magnetic scalar potential in the data set and vary the mesh element size. The values evaluated at four points with coordinates (-1.58, 27.8) cm (blue), (-1.59, 27.8) cm (green), (1.58, 27.4) cm (red) and (1.57, 27.4) cm (cyan) in the data set are shown:

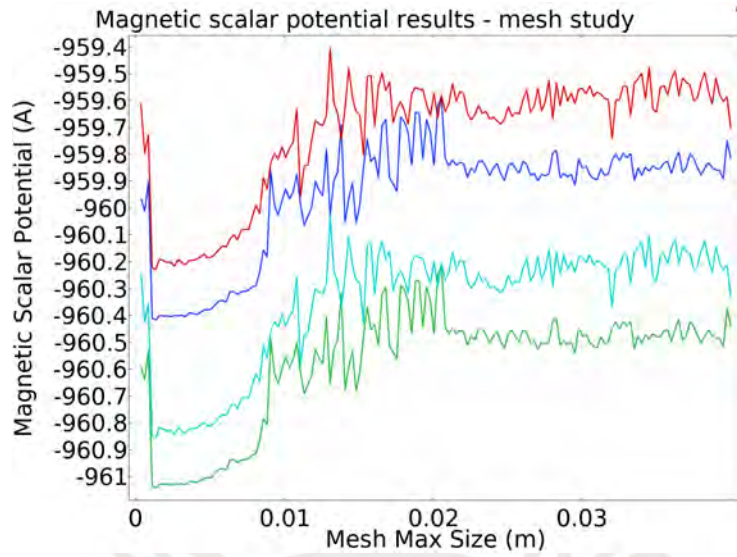


Figure 3.9: Magnetic scalar potential evaluated in four points

As we can observe, from mesh sizes smaller than 0.02 m the error increases and the values for the magnetic scalar potential (V_m) drops one decimal point. The mean of the standard deviation values of the magnetic scalar potential evaluated at all points for mesh sizes smaller than 0.02 m is 0.25 and for sizes greater than 0.02 m the standard deviation is 0.05.

In the last case, we compute the magnetic field norm $\|\mathbf{B}\|$ in every point of the data set for different mesh sizes. The values evaluated at four points with coordinates (0.17, 28.2) cm (blue), (0.28, 28.2) cm (green), (0.17, 28.3) cm (red) and (0.17, 28.3) cm (cyan) are shown:

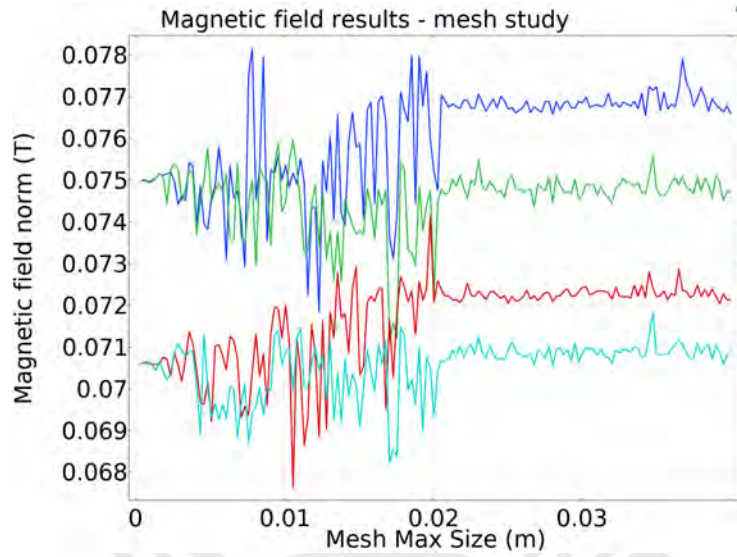


Figure 3.10: Magnetic field evaluated in four points

As in all previous cases, the numerical noise decreases for mesh size greater than 0.02 m. The mean of the standard deviation values of the magnetic field norm evaluated at all points for mesh sizes smaller than 0.02 m is 0.01 and for sizes greater than 0.02 m the standard deviation is 0.0002. Now we need to determine the mesh size that minimizes the error of the solutions of the fields at each point of the data set. For this, we will consider that the error range of each solution is not greater than three times the standard deviation from the mean, in other words, solutions must be in the range of $[\mu - 3\sigma, \mu + 3\sigma]$. In the next figure we show the error of each variable:

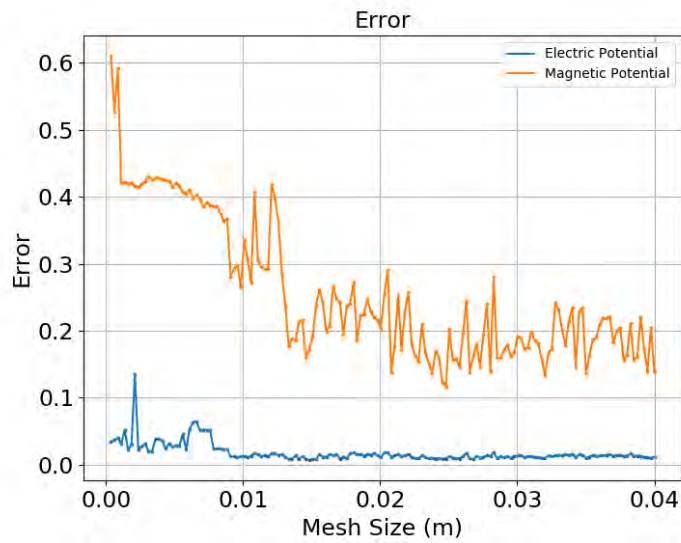


Figure 3.11: Error of the solutions vs mesh size for the electric potential and the magnetic scalar potential

We now show the relation between the mesh size and, the execution time and the number of degrees of freedom. These results were obtained by running the simulations on a computer with 16 GB of RAM, 500 GB of HDD memory and 2.60GHz of clock speed.

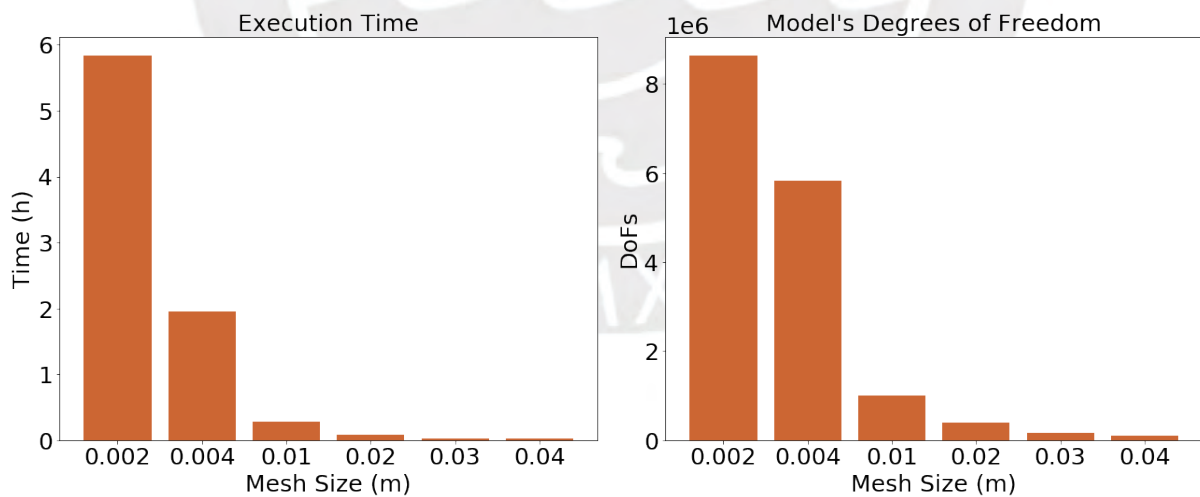


Figure 3.12: Execution time and degrees of freedom vs mesh size

Mesh Max Element Size (mm)	2.0	4.0	10.0	20.0	30.0	40.0
Mesh Min Element Size (mm)	9.00E-04	1.00E-03	0.5	0.9	1.8	3.0
Number of Mesh Elements	6.45E6	4.36E6	7.49E5	2.90E5	1.18E5	7.19E4
Execution Time	5h 50min	1h 57min	17 min	5 min	2 min	1 min
Degrees of Freedom	8.63E6	5.83E6	1.0E6	3.89E5	1.59E5	9.68E4
Memory (GB)	9.53	8.72	5.47	3.37	2.69	2.56

Table 3.2: Table of mesh study parameters and results

As we can observe the execution time of the model with a mesh maximum size of 2.0 mm can take up to 5 hours and 50 minutes while using a mesh maximum size of 40.0 mm can take 1 minute. Additionally, the HDD file size drops from 9.53 GB to 2.56 GB, HDD size saving is an important parameter to consider in the selection of the mesh size and distribution. With this information we can calculate the optimal maximum and minimum element sizes for modeling the magnetron system. From the margin of error established the optimal maximum mesh size calculated is 20.0 mm. This size will be used in all the simulations presented in this work. The final mesh used is shown in the following figure:

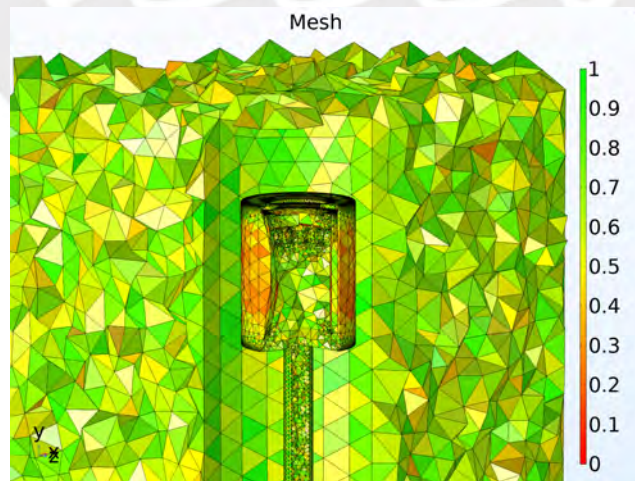


Figure 3.13: Final mesh size

The color in figure 3.13 represents a measure of how much the angles in each tetrahedral

element deviates from a regular tetrahedron. This measure, represented by a number between 0 and 1, indicates the quality of the mesh element, with 0 representing the worst quality and 1 the best quality. This parameter is important to validate the simulation results and get accurate results [12, 13].

3.3. Results

The mesh element type that was used to discretize the geometry was the free tetrahedral default option. It is the simplest type of element that can adapt to any type of geometry. Once the mesh element type, optimal minimum mesh size and maximum mesh size are determined we calculate the electric potential, electric field, magnetic field, particle trajectories and particle velocity distributions.

3.3.1. Electric Potential and Electric Field

As shown in figure 3.1 the internal structure of the magnetron is connected to a radio-frequency source operating at 13.56 MHz with a power range from 20 W to 110 W and the maximum voltage that the electrode generates is 195 V. So, the boundary condition we establish to describe the electric potential is

$$V(t) = 195 \cos(\omega_{RF}t), \quad \omega_{RF} = 2 * \pi * 13.56 \text{ MHz} \quad (3.1)$$

For a two dimensional cut of the magnetron at a time $t = 0$, the electric potential has as a symmetric spatial distribution shown in figure 3.14.

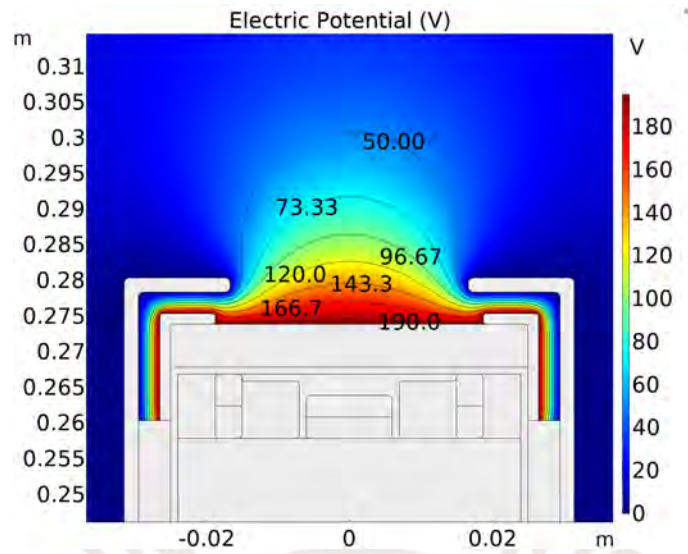


Figure 3.14: Electric potential distribution

In color is shown the value of the electric potential and some equipotential curves are plotted with their respective values. Near the cathode, the electric potential is near 195 V and as the distance from the target increases the electric potential decreases. On the other hand, we plot the electric potential and the electric field vector distribution in figure 3.15.

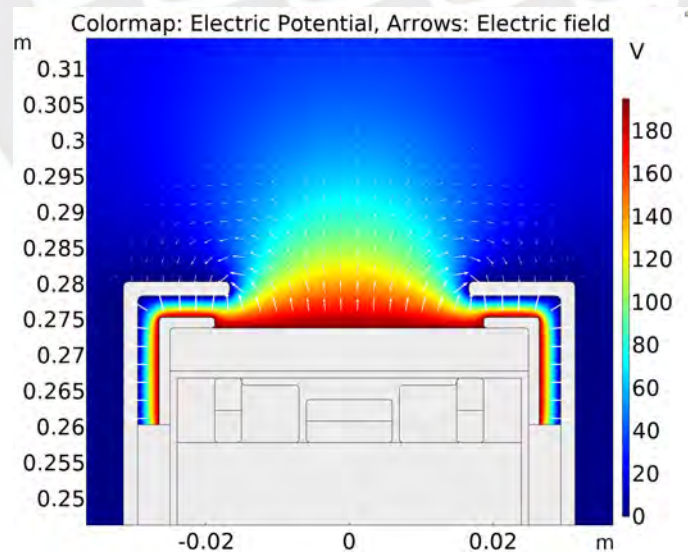


Figure 3.15: Electric field distribution

3.3.2. Magnetic Field

To calculate the magnetic field generated by the pair of permanent neodymium magnets we define a magnetization vector for the internal and external magnets. The internal magnet has a value of

$$\mathbf{M} = (0, 0, 650) \frac{\text{kA}}{\text{m}} \quad (3.2)$$

The external magnet has a value of

$$\mathbf{M} = (0, 0, -650) \frac{\text{kA}}{\text{m}} \quad (3.3)$$

Both magnets have the same magnetization value in different directions so that the magnetic field is closed and the electron trap region can be simulated. For a two dimensional cut of the magnetron, the simulation results are shown in figure 3.16.

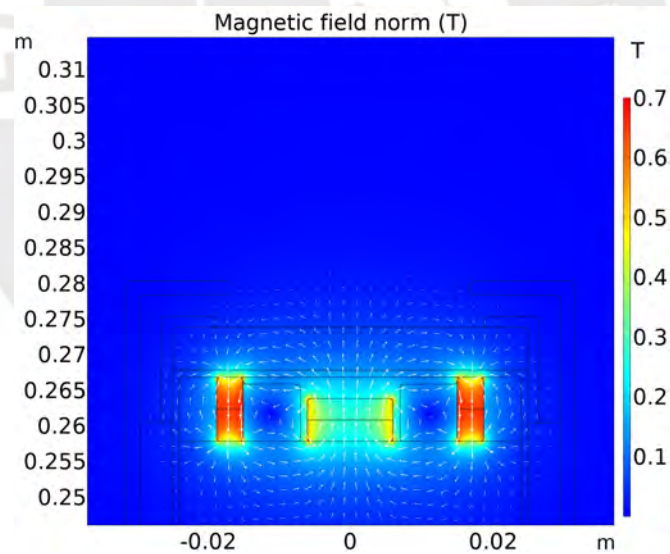


Figure 3.16: Magnetic field norm distribution

In color scale the magnetic field norm distribution is plotted and in arrows the magnetic field direction and magnitude. In the surface and interior of the magnets the magnetic field has a top value of 0.7 T and in the surface of the target, located between coordinates (-0.01925, 0.27382)

m and (0.01925, 0.27382) m the magnetic field has a peak value of 0.055 T.

3.3.3. Particle Trajectories

Charged particle motions as mentioned in Chapter 2 are modeled by the Lorentz force, in which the electric field and magnetic field present in equation 2.6 are calculated by the magnetron's electrodes and magnets [6]. The first and more simple approach to model the Argon ion and electron motions present in the sputtering plasma is to ignore the collisions between the electrons and ionized argon atoms with the background gas (Argon) and also ignore the recalculation of the electric and magnetic fields due to the current and charge densities of the particles in the plasma [8].

The first approach consists in calculating the electric and magnetic field spatial distributions generated by the magnetron and then the electron trajectories. Since the electron mass is about 10^4 times more lighter than Argon ions mass, the mean velocity of electrons is many orders of magnitude higher than of Argon and the Larmor radius is much larger for ions, so it is not suitable to simulate both particles simultaneously [14, 15]. We reproduced the electron trap region in our simulation, in figure 3.17 we show the result at time $t = 1.39\text{E}-7\text{s}$. The electron trap, a region where electrons are confined because of the magnetic field, is formed due to the $\mathbf{E} \times \mathbf{B}$ drift, both the electric and magnetic fields are perpendicular, so a drift velocity in the azimuthal direction is generated in the surface of the target. Hence an azimuthal electric current is generated due to the Hall effect [16].

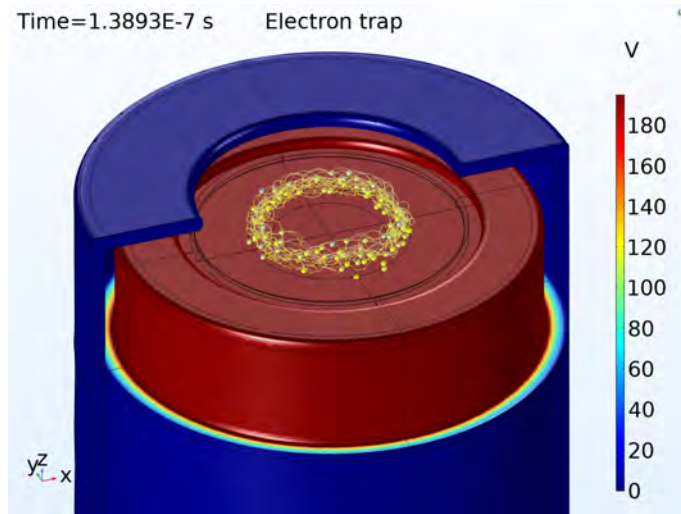


Figure 3.17: Electron transport in the surface of the target due the Hall Effect

To visualize this effect in a more detailed way, figure 3.18 shows the Poincaré map of the electron trajectories. We performed a 2D plane cut in the x-y axis at $z = 0.276$ m. The Poincaré map shows the coordinates of the particles in the plane at all time steps smaller than $t = 1.47E-7$ s.

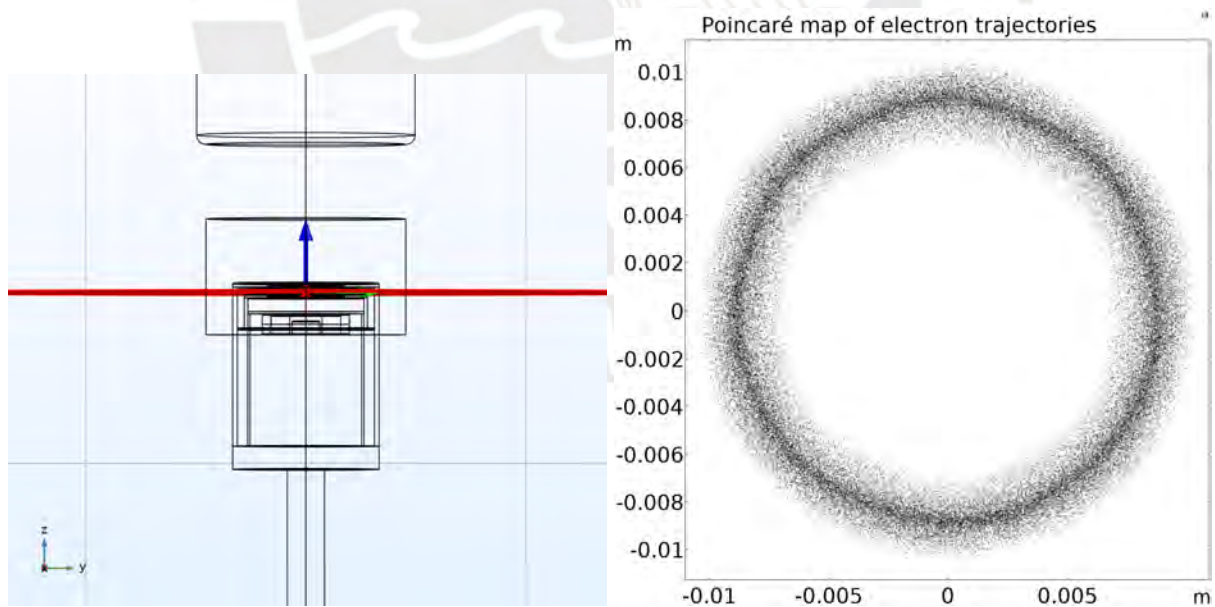


Figure 3.18: Cut plane at $z = 0.276$ m and the Poincaré map of electron trajectories

The dots in the Poincaré maps are the result of a simulation of 10000 electrons with random

initial velocities and positions near the target. The electrons travel in an azimuthal direction in the magnetic trap region. This effect is of great importance in the sputtering technique because the free electrons generated at the target surface, in the magnetic trap region, collide multiple times with the background gas and ionize a large number of neutral particles that are responsible of the collisions with the target material [2].

For the second approach or level of complexity in the particles simulations, we will consider the collisions between electrons and the background gas, in this case Argon. Three types of collisions have been taken in consideration: Elastic collisions, excitation and ionization. In table 3.3 we show the three collisions processes and the energy loss for each reaction.

Reaction	Type	Energy Loss (eV)
$\text{Ar} + e \rightarrow \text{Ar} + e$	Elastic Collision	0.0
$\text{Ar} + e \rightarrow \text{Ar}^* + e$	Excitation	11.548
$\text{Ar} + e \rightarrow \text{Ar}^+ + 2e$	Ionization	15.80

Table 3.3: Collision types considered in the particle simulation [17]

The first type of collision is the elastic collision, an electron collides with a neutral Argon atom and changes direction, but the internal energies of the particles are not modified in the process. The other two reactions are called inelastic collisions, in these cases the total kinetic energy after the reaction is less than the initial total kinetic energy. In the case of the excitation reaction an electron collides with an Argon atom, changes direction and some energy is transferred to the ion leading to loss of electron energy. The third process is the ionization collision, the electron collides with an Argon atom, an ionized particle and a second electron are produced, with momentum energy transfer [18].

To model numerically the atomic collisions the cross section parameter must be taken into account. This parameter describes the effective area of the particle-particle interaction and depends on the angle of incidence and incident particle energy [18]. For this simulation, the cross sections for Argon as a function of the incident electron energy have been calculated and used

from a validated free online resource [19]. In figure 3.19 the cross sections are shown for each reaction as a function of the incident electron energy.

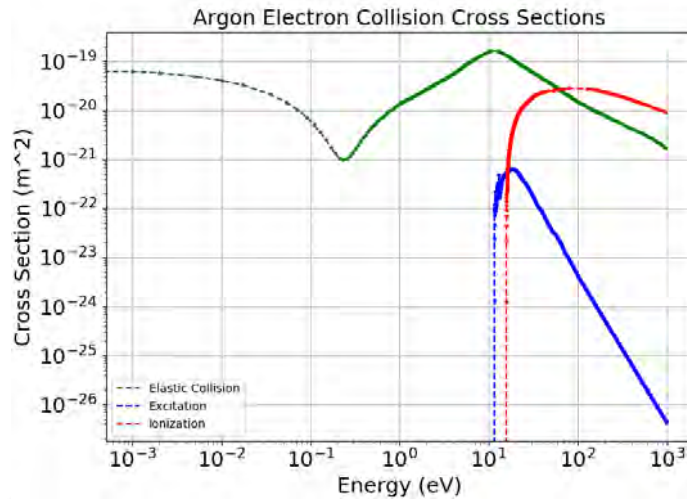


Figure 3.19: Argon cross sections for elastic, excitation and ionization reactions [19]

In the case of the elastic collision, the electron has a wider range of energies for which it can interact. This is due to the fact that no energy is transferred in the collision, so there is no need of a threshold value to excite certain quantum state in the target atom. In the case of the excitation and ionization a minimum electron energy is required to carry out the reaction [18].

The algorithm for determining the probability of a collision taking place is called the Monte Carlo collision method. This method consists in considering that a particle of species s , in this case an electron, has N possible collisions, three collisions in this case, with the target or background species. For the i th incident particle the kinetic energy is determined by

$$\epsilon_i = \frac{1}{2} m_s v_i^2 \quad (3.4)$$

Then, this energy is required to calculate the total cross section

$$\sigma_T(\epsilon_i) = \sum_{k=1}^N \sigma_k(\epsilon_i) \quad (3.5)$$

The total cross section is the sum of all the individual cross sections considered in the simulation. Here, $\sigma_k(\varepsilon_i)$ for $1 \leq k \leq N$ is the k th type of reaction between the incident species s and the background species. Taking into account the distance $\Delta s_i = v_i \Delta t$ that the incident particle has traveled in the time step Δt , the collision probability between the incident particle and the target species is calculated as follows

$$P_i = 1 - \exp(-v_i \Delta t \sigma_T(\varepsilon_i) n_t(\mathbf{x}_i)) \quad (3.6)$$

Where $n_t(\mathbf{x}_i)$ is the background density as a function of the position. A uniformly distributed random number U in the interval $(0,1)$ is generated, if $U \leq P_i$ the collision occurs and then another random number is generated to determine the type of collision [20, 21].

In the following simulation, the three magnetrons have been built and positioned with approximate measurements taken at the laboratory. The electric and magnetic field spatial distributions have been calculated and 120'000 electrons have been introduced in the simulation. Elastic collisions, excitation and ionization reaction functions have been considered. The data points were calculated using the open-access website LXCat, an open source project developed to model low temperature plasmas [19]. Then, the extracted points have been interpolated to obtain three continuous functions. The background number density considered is a constant value of $n_{BG} = 1E15 \text{ 1/m}^3$ and the simulation runs until $t = 2.95E-7 \text{ s}$, equal to the time of four RF cycles. More simulation time leads to exceedingly high execution time and a lot of RAM memory occupation. In figure 3.20 is shown the geometry of the three magnetrons.

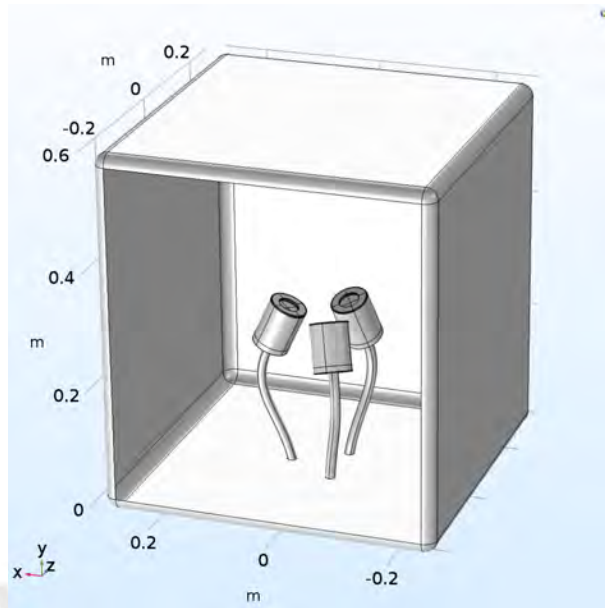


Figure 3.20: System of three magnetrons

In the real design developed at the laboratory each magnetron is inclined at an angle of 25 degrees above the horizontal plane and are positioned symmetrically. On top of the three magnetrons is positioned the substrate where the sputtered material is deposited. In this design and simulation, the substrate has not been considered, only the magnetrons and the effect in the electron trajectories. In figure 3.21 is shown the electron velocity distribution at final time $t = 2.95E-7$ s.

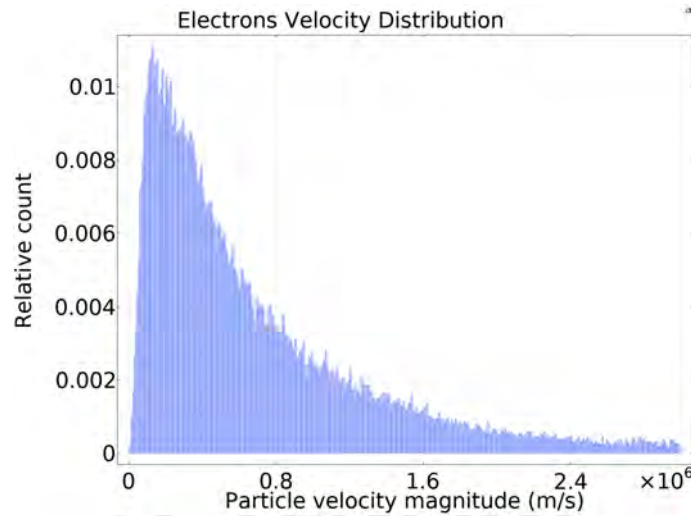


Figure 3.21: Electrons velocity distribution

Electrons are initially randomly positioned throughout the domain with initial velocities normally distributed with mean 0 m/s and standard deviation of 10'000 m/s. Electrons suffer different types of collisions depending on their kinetic energies at each time step. The effect of collisions in each electron is a discrete discontinuity in the velocity and position of the electron leading to a stochastic random walk [21]. As seen in the velocity distribution plot, fig 3.21, at a final time the distribution has a peak at a velocity of electrons of $v = 1.2E5$ m/s or energy equivalent to $E = 0.04$ eV. Comparing this value to figure 3.19 most of the electrons in the simulation do not have sufficient energy to ionize or excite Argon atoms, only sufficient energy to collide elastically with the background gas. In a more complicated simulation, more effects like the electric potential recalculation and the magnetic field recalculation has to be taken into account.

3.3.4. Fluid simulation of a capacitively coupled plasma

A capacitively coupled plasma (CCP) is a type of low temperature plasma that is generated by the discharge of an inert gas like Argon or Neon between a pair of electrodes. Typically, one electrode is powered by a sinusoidal radio frequency source and the other is connected to

ground. Both electrodes are circular plates separated by a gap in the range $0.5 \leq d_{\text{gap}} \leq 4$ cm, typical radio frequency operations are in the range of $1 \leq f_{\text{RF}} \leq 100$ MHz and voltage power in the range of $50 \text{ V} \leq V_0 \leq 100$ kV. The size and pressure of the chamber plays an important role in the electron dynamics inside the plasma, with high pressure, electrons have less mobility due to collisions and all the energy is deposited in the bulk region [22]. Magnetrons have a similar discharge, however in this case a static magnetic field is applied to confine the plasma near the target [15]. Figure 3.22 shows the schematic design of a CCP, the top electrode is connected to ground and the bottom electrode is connected to the RF-generator, the whole system is in a vacuum and a gas mixture is injected, in the center is located the bulk region and near the electrodes a plasma sheath is formed [22].

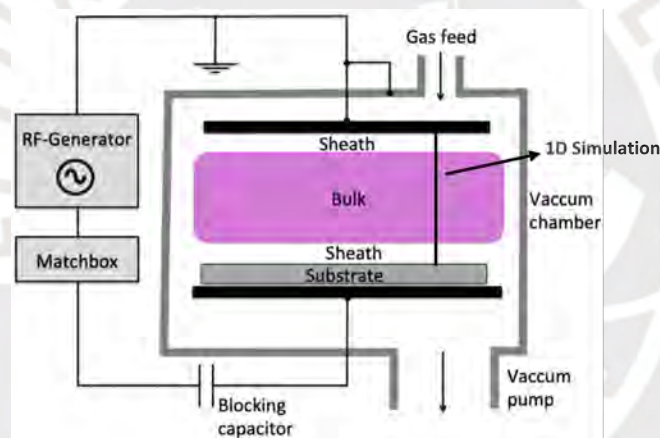


Figure 3.22: Diagram of a CCP [22]

One theoretical approach to model these types of plasmas is by the use of a computational fluid model. In section 2.3 the basic equations are described and are the ones implemented in COMSOL's Plasma Module [10]. A 1D simulation have been performed in order to validate and study the properties of the CCP. The geometry consists in a line cut through the plasma where each end of the line is connected to each electrode as shown in figure 3.22. The bottom end of the line is the contact connected to the RF source and the top end of the line is the contact connected to ground. The initial conditions and chamber parameters that have been considered are an electrode gap of $d_{\text{gap}} = 2.5$ cm, electrode disk radius of $r_{\text{electrode}} = 15$ cm, radio frequency power

of $f_{RF} = 13.56$ MHz, pressure of $p_0 = 133$ Pa, initial gas temperature of $T_0 = 300$ K, applied power of 80 W and initial electron density of $1E14$ $1/m^3$. The three main reactions considered between Argon and electrons in the simulation are specified in table 3.3 and in figure 3.19. To solve the system of equations of a RF CCP the equations must be solved for a large integration time, in the order of 10000 cycles. To address this problem, COMSOL approaches the solution by solving the system of equations in the frequency domain, all solutions are the result of the average over one period or cycle [10].

Figure 3.23 shows the results of the electron density profile as a function of the distance between the electrodes.

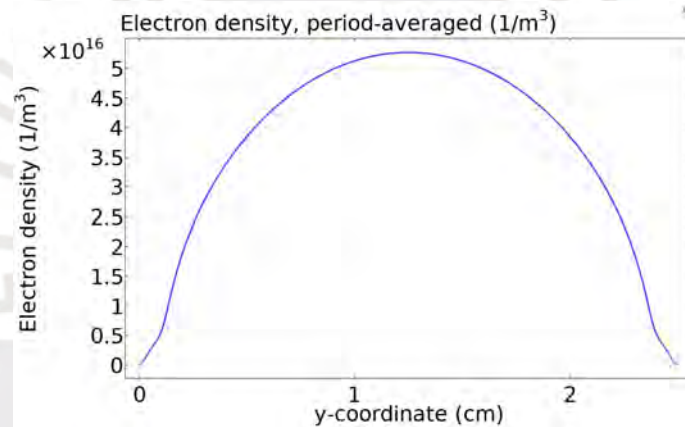


Figure 3.23: Electron density profile as a function of the distance

As can be seen near the electrodes, the density drops to zero and in the center region the density increases. This occurs because electrons traveling from one electrode to another lose all their energy in the bulk region through collisions, therefore, a higher density and accumulation of electrons is generated in the center [23]. In figure 3.24 is shown the electron temperature profile.

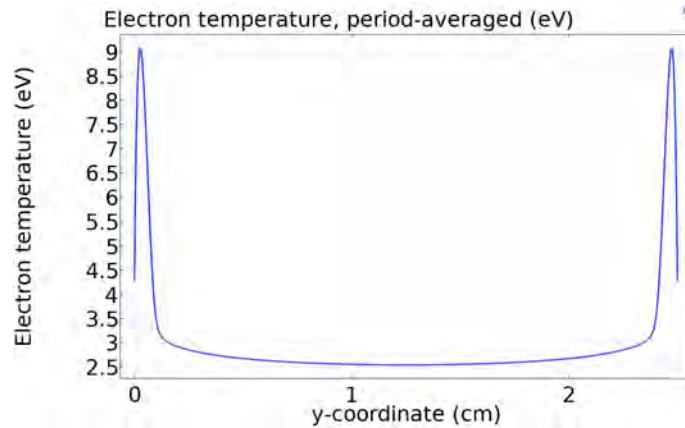


Figure 3.24: Electron temperature profile as a function of the distance

As can be seen, near the electrodes the electron temperature increases up to 9 eV, and in the center it drops to 2.5 eV. This happens because near the electrodes the electric field is higher due to the change in voltage, so electrons have higher kinetic energy in these regions. While traveling to the central region they lose all their energy through collisions, therefore their temperature drops [23]. Finally, in figure 3.25 the electric potential in blue (left y-axis) and the electric field in green (right y-axis) profiles are shown.

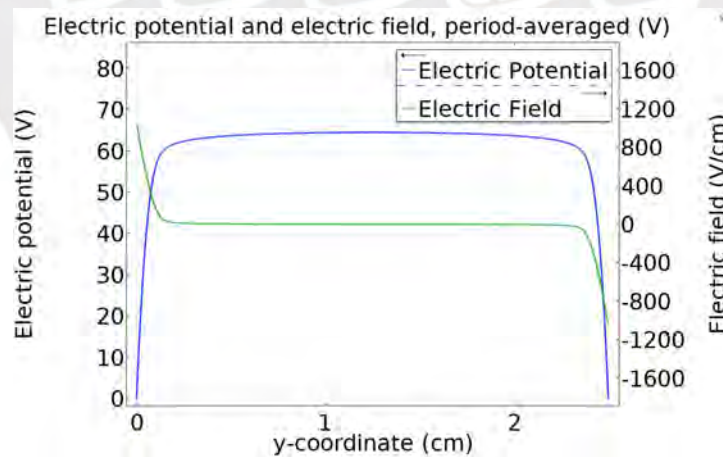


Figure 3.25: Electric potential and electric field profiles as a function of the distance

As can be seen from the figures, near the electrodes the potential drops to zero, in the top end of the chamber, due to the ground voltage value of 0 V and in the bottom end of the chamber because the average voltage in a period of one RF cycle is 0 V. In the center the potential takes

the value of the plasma potential. The region where the potential gradient or the electric field starts to increase or decrease is called the plasma sheath region, this region forms because of the difference in the density of electrons and positive ions. Electrons as shown in figure 3.23 accumulate in the center region of the chamber, this generates a large charge separation between the center and the extreme sides, therefore an electric field is formed.



Chapter IV

Conclusions

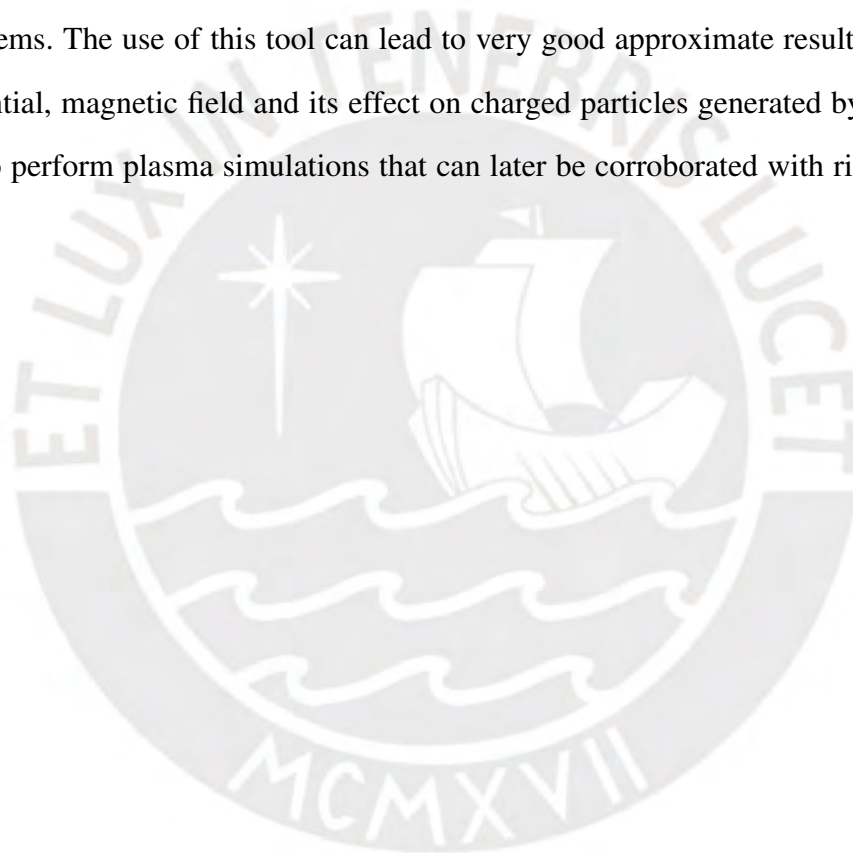
In the present project the finite element method has been implemented to solve the electric field, electric potential, magnetic field and magnetic scalar potential distributions of a magnetron system design at the MatER laboratory of the Pontificia Universidad Católica del Perú. The numerical simulation has taken into consideration the corresponding initial conditions and boundary conditions necessary to solve Maxwell's equations and a numerical error study has been carried out in order to minimize the error in the solutions and optimize the solution time.

The solutions for the fields were used later to calculate the electron trajectories by the use of the Lorentz force and a Monte Carlo collisions method. The effect of the magnetic trap near the target was recovered and the electron velocity distribution (EVD) was calculated. On the other hand, more complicated simulations can be performed, for instance, considering ions and electrons in the simulation and taking into account the particle-particle interaction and the particle-field interactions. Due to the difference in mass and velocities, running a simulation that considers both particles will require a very small step size to recover the electron trajectories and a large integration time to recover the ion dynamics, leading to a large number of calculations and computational power. Nevertheless, important physics phenomena and insights can be recovered through the use of particle tracing simulations.

Finally, to study the computational fluid model of a plasma, a simulation of a capacitively

coupled plasma was developed. By studying this system, basic properties of a two-electrode system were recovered, such as the electron density, the electron temperature and the electric potential distributions. These basic results are a starting point for more complicated simulations in two or three dimensions, taking into account the magnetic field of the magnetron and the complicated geometry configuration.

In conclusion, the finite element method implemented in COMSOL Multiphysics is a suitable and powerful method to obtain fast and validated computational results from complicated physical systems. The use of this tool can lead to very good approximate results to obtain the electric potential, magnetic field and its effect on charged particles generated by very detailed devices, or to perform plasma simulations that can later be corroborated with rigorous experiments.



Bibliography

- [1] Martin, P., 2010. *Handbook Of Deposition Technologies For Films And Coatings*. 3rd ed. Oxford, U.K.: William Andrew/Elsevier, pp.253-294.
- [2] Braun, P., 2014. Magnetron Sputtering Technique. *Handbook of Manufacturing Engineering and Technology* (pp. 2929-2957). England, U.K.: Springer.
- [3] Chen, F., 2015. *Introduction to Plasma Physics and Controlled Fusion*. 3rd ed. Los Angeles, USA: Springer, pp.1-18.
- [4] *Detailed Explanation of the Finite Element Method (FEM)*. Comsol.com. (2020). From <https://www.comsol.com/multiphysics/finite-element-method>.
- [5] AC/DC Module User's Guide. COMSOL Multiphysics® v. 5.4. COMSOL AB, Stockholm, Sweden. 2018
- [6] Chen, F., 2015. *Introduction to Plasma Physics and Controlled Fusion*. 3rd ed. Los Angeles, USA: Springer, pp.19-49.
- [7] Colonna, G., 2016. Boltzmann and Vlasov equations in plasma physics. *Plasma modeling: methods and applications* (pp. 1-23). England, U.K.: IOP Publishing.
- [8] Gurnett, D.A., Bhattacharjee, A., 2005. *Introduction to Plasma Physics: With Space and Laboratory Applications*. 1st ed. Cambridge, U.K.: Cambridge University Press, pp.137-174.

- [9] H. Kim, F. Iza, S. Yang, M. Radmilović-Radjenović and J. Lee, "Particle and fluid simulations of low-temperature plasma discharges: benchmarks and kinetic effects", *Journal of Physics D: Applied Physics*, vol. 38, no. 19, pp. R283-R301, 2005. DOI: 10.1088/0022-3727/38/19/r01.
- [10] Plasma Module User's Guide. COMSOL Multiphysics® v. 5.4. COMSOL AB, Stockholm, Sweden. 2018
- [11] *Online Materials Information Resource - MatWeb*. Matweb.com. (2020). From <http://www.matweb.com/>.
- [12] *How to Inspect Your Mesh in COMSOL Multiphysics®*. COMSOL Multiphysics. (2021). From <https://www.comsol.com/blogs/how-to-inspect-your-mesh-in-comsol-multiphysics/>.
- [13] COMSOL Multiphysics Reference Manual. COMSOL Multiphysics® v. 5.5. COMSOL AB, Stockholm, Sweden. 2019
- [14] T. E. Sheridan, M. J. Goeckner, and J. Goree, "Electron and ion transport in magnetron plasmas", *Journal of Vacuum Science & Technology A: Vacuum, Surfaces, and Films*, vol. 8, no. 3, pp. 1623-1626, 1990. DOI: 10.1116/1.576776.
- [15] T. Charoy, J. Boeuf, A. Bourdon, J. Carlsson, P. Chabert, B. Cuenot et al., "2D axial-azimuthal particle-in-cell benchmark for low-temperature partially magnetized plasmas", *Plasma Sources Science And Technology*, vol. 28, no. 10, pp. 105010, 2016. DOI: 10.1088/1361-6595/ab46c5.
- [16] A. Anders, "Discharge physics of high power impulse magnetron sputtering", *Surface And Coatings Technology*, vol. 205, pp. S1-S9, 2011. DOI: 10.1016/j.surfcoat.2011.03.081.
- [17] M. Becker, H. Kählert, A. Sun, M. Bonitz, & D. Loffhagen, "Advanced fluid modeling and PIC/MCC simulations of low-pressure ccrf discharges", *Plasma Sources Science And Technology*, vol. 26, no. 4, pp. 044001, 2017. DOI: 10.1088/1361-6595/aa5cce.

- [18] Lieberman, M., & Lichtenberg, A., 2006. Atomic Collisions. *Principles of Plasma Discharges and Materials Processing* (2nd ed., pp. 43-85). USA: John Wiley & Sons.
- [19] *About the project*. Fr.lxcat.net. (2020). From <https://fr.lxcat.net/home/>.
- [20] V. Vahedi, & M. Surendra, "A Monte Carlo collision model for the particle-in-cell method: applications to argon and oxygen discharges", *Computer Physics Communications*, vol. 87, no. 1-2, pp. 179-198, 1995. DOI: 10.1016/0010-4655(94)00171-w.
- [21] Particle Tracing Module User's Guide. COMSOL Multiphysics® v. 5.4. COMSOL AB, Stockholm, Sweden. 2018
- [22] Wilczek, S., Schulze, J., Brinkmann, R., Donkó, Z., Trieschmann, J., Mussenbrock, T. "Electron dynamics in low pressure capacitively coupled radio frequency discharges", *Journal Of Applied Physics*, vol. 127, no. 18, pp. 181101, 2020. DOI: 10.1063/5.0003114.
- [23] Hwang, S., Lee, H., Lee, H. "Effect of electron Monte Carlo collisions on a hybrid simulation of a low-pressure capacitively coupled plasma", *Plasma Sources Science And Technology*, vol. 23, no. 6, pp. 065040, 2014. DOI: 10.1088/0963-0252/23/6/065040